CrossMark

Growth, structural, optical, thermal, laser damage threshold and theoretical investigations of organic nonlinear optical 2-aminopyridinium 4-nitrophenolate 4-nitrophenol (2AP4N) single crystal

P. Karuppasamy[1] · T. Kamalesh[1] · C. Senthil Kumar[1] · Muthu Senthil Pandian[1] · P. Ramasamy[1] · Sunil Verma[2,3] · S. Venugopal Rao[4]

Abstract

The good quality organic 2-aminopyridinium 4-nitrophenolate 4-nitrophenol (2AP4N) single crystals with the dimension of $30 \times 5 \times 5$ mm^3 have been grown by slow evaporation solution technique (SEST) at ambient temperature within the period of 30 days using methanol as solvent. Initially, the structure of grown 2AP4N single crystal was confirmed by the single crystal X-ray diffraction (SXRD). Intermolecular interactions of 2AP4N molecule were analyzed by Hirshfeld surface analysis. The grown crystal was studied by powder X-ray diffraction (PXRD) measurement, it has sharp peaks which indicates good crystallinity. The presence of various functional groups have been confirmed by FTIR and FT-Raman spectra analysis. The optical quality (transparency) of the grown crystal was studied by UV–Vis NIR spectral analysis and it has good optical transparency in the visible and near IR regions with the cut-off wavelength of 470 nm. The energy values of highest occupied molecular orbital (HOMO) and lowest unoccupied molecular orbital (LUMO) have been calculated. The density of states (DOS) spectra was used to study the bonding, anti-bonding and non-bonding interactions. The Mulliken charge distribution was used to confirm the sign and magnitude of charge of each atom. The distribution of charge and its related properties were analyzed by the molecular electrostatic potential (MEP). The natural bonding orbital (NBO) theory was used to analyse the inter-intra molecular interactions of 2AP4N. First-order hyperpolarizability (β_{total}) of 2AP4N molecule was found to be 1.071^{-29} esu, which is 28.6 times that of urea. Photoluminescence measurement reveals that the 2AP4N crystal has very high emission at 500 nm. The thermal stability of grown crystal was found to be 90 °C. The dislocation density was analyzed and it was confirmed to possess less defects. The laser damage threshold (LDT) energy has been measured by using Nd: YAG laser (532 nm). The efficiency of second harmonic generation (SHG) of grown 2AP4N was evaluated by Kurtz-Perry powder technique. The SHG efficiency of 2AP4N was found to be 4.5 times that of standard KDP material. The high SHG values of 2AP4N crystals may be more favorable for nonlinear optical (NLO) device applications.

1 Introduction

Nonlinear optical (NLO) materials have attracted much attention because of their wide applications. Among all the NLO materials, organic materials are considered to be more

✉ P. Karuppasamy
  karuppasamyp75@gmail.com; karuppasamyp@ssn.edu.in

[1] SSN Research Centre, SSN College of Engineering, Chennai, Tamil Nadu 603110, India

[2] Laser Materials Development and Devices Division, Raja Ramanna Centre for Advanced Technology (RRCAT), Indore, Madhya Pradesh 452013, India

[3] Homi Bhabha National Institute, Anushakti Nagar, Mumbai, Maharashtra 400094, India

[4] Advanced Centre of Research in High Energy Materials (ACRHEM), University of Hyderabad, Gachibowli, Hyderabad, Telangana 500046, India

versatile for their potentially high nonlinearities and rapid response compared with inorganic compounds. The organic NLO crystals have gained many applications in the broad areas such as laser technology, electro-optic switches, color displays, frequency conversion, optical parametric oscillations, optical data storage and etc., [1–3]. The organic materials are expected to have relatively strong nonlinear optical properties due to the presence of delocalized π-electrons conjugate system, connecting both donor and acceptor (D–A) groups responsible for enhancing their asymmetric polarizability. Other advantages of organic compounds are amenability for synthesis, multifunctional substitutions, higher resistance to optical damage and maneuverability for device applications [4]. Finding ways to ensure that a bulk material is acentric has been a serious hurdle in the design of new organic materials with non-centrosymmetric packing for NLO uses. The organic materials of aminopyridines (AP) are significant class of bioactive N-heterocyclic amines, which increase the strength of nerve signals. On the other hand, their unique chemical and physical properties lead towards catalysts and reagents in organic synthesis, light-emitting diodes (LED), synthesis of intense fluorescence dyes and nonlinear optical applications [5]. Aminopyridines are commonly presented in synthetic and natural products [6]. They are formed by ordinary moieties in many huge molecules with intriguing photo-physical, electrochemical and catalytic properties owing to their excellent electron–acceptor constituent (amino group). It is a heterocyclic molecule containing two nitrogen atoms which are used to identify its nucleic acid basis. It is used in the synthesis of pharmaceuticals especially for antihistamines, anti-inflammatories and other drugs. At present, the investigations on 2-aminopyridine (2AP) complex of organic materials are interesting for optoelectronic applications. On the other hand, 4-nitrophenol (4NP) is a highly needed and interesting candidate, as they are a typical one-dimensional (1D) donor–π–acceptor (D–π–A) system, and the presence of phenolic group (OH) favours the formation of salts easily with various organic and inorganic systems. Moreover, it consists of both nitro (acceptor group) and hydroxyl (donor group) in opposite sites. The 4NP has both classic dipolar NLO chromophore, D–π–A system and hence the more chance to get proton transfer from the phenolic (OH) to various organic bases. The conjugated base, phenolate, thus formed has increased molecular hyperpolarizability because of the better electron donating character of phenolate O– (Hammett coefficient $\sigma = -0.81$) [7] than that of phenolic OH (Hammett coefficient $\sigma = -0.38$) [8] and it can increase the molecular hyperpolarizability [9]. In recent years, some pyridinium and nitrophenolate based NLO complexes were synthesized and their fascinating NLO properties are reported [10–12]. Moreover, the pyridine is an efficient group, can increase the number of π electrons as well as their delocalization

resulting in increasing NLO efficiency. If a proton transfer between two separate NLO organic chromophores takes place and if it results in a non-centrosymmetric organic material, this can increase the hyperpolarizability of both the 2AP and 4NP species.
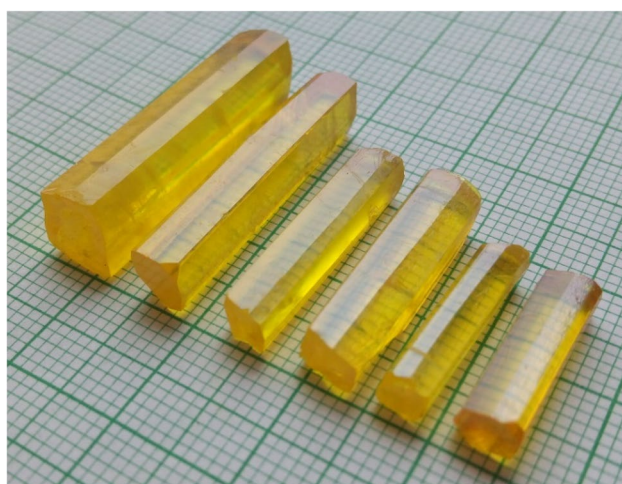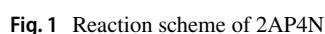
When the 2AP is added to the 4NP in the 1:2 molar ratio, the hydroxyl group of 4NP is protonated to the organic heterocyclic molecule of 2AP, which acts as acceptor and this protonated molecule is combined to third partner of neutral molecule of 4NP. Normally, the organic materials are having poor thermal, chemical and mechanical stability [13]. These are overcome to achieve the good macroscopic organic crystals with higher nonlinearity due to an increase in the number of π electron delocalization, which improves the molecular hyperpolarizability. These materials have particular features, such as weak van der Waals (*vdW*) and hydrogen bonds, wide transparency ranges in the visible regions and zwitterionic nature [14]. Normally, acentric molecules consist of highly delocalized π electron systems interacting with suitable D–π–A system and it exhibits a high value of second order polarizability (β). Theoretical investigation is essential for finding the materials for specific applications. Hence, these are projected as forefront candidates for the fundamental and applied investigations.

In the present work, a systematic investigation has been carried out on the growth and characterization of 2-aminopyridinium 4-nitrophenolate 4-nitrophenol (2AP4N) single crystals. The grown crystal was analyzed by various theoretical approaches and it was subjected to different characterization techniques such as single crystal X-ray diffraction (SXRD), powder XRD (PXRD), UV–Vis NIR analysis, photoluminescence (PL) studies, TG-DTA, chemical etching, laser damage threshold (LDT) and SHG measurement.

2 Experiment

2.1 Material synthesis, crystal growth and morphology

The analytical reagent (AR) grade raw materials of 2-aminopyridine (2AP) and 4-nitrophenol (4NP) were taken in the stoichiometric ratio of 1:2 for the synthesis of organic 2-aminopyridinium 4-nitrophenolate 4-nitrophenol (2AP4N) compound. Initially, the calculated amount of 2AP and 4NP were taken in high purity methanol solvent. The solution was continuously stirred until it reached the homogeneous condition. After that, it appeared as clear reddish color. The prepared solution (charge material) was filtered twice by using Whatman filter paper and then it was transferred into the crystallizing dish (glass). The dish was covered by a thick polythene sheet and then after 1 day, few tiny holes was made on the polythene sheet for allowing controlled

2-Aminopyridine **4-Nitrophenol** **2-Aminopyridinium 4-nitrophenolate 4-nitrophenol**

Fig. 1 Reaction scheme of 2AP4N

Fig. 2 As grown 2AP4N single crystal

Fig. 3 Morphology of 2AP4N single crystal

evaporation at ambient temperature. After some days, the bright yellow colored 2AP4N single crystals were formed randomly. These crystals were harvested before the complete evaporation of solvent, because final stages solution is always contains some impurities. Then the harvested crystals were again washed using the purified methanol solvent to remove any adsorbed impurities on the crystal surface. The quality of crystalline materials was further improved by successive recrystallization process (conventional crystal growth process repeated several times). The optically transparent 2AP4N crystals with the dimension of $30 \times 5 \times 5$ mm^3 have been grown in a period of 30 days by slow evaporation solution technique (SEST). The reaction scheme of 2AP4N material is depicted in Fig. 1. SEST grown 2AP4N crystals are shown in Fig. 2. The morphology of 2AP4N was indexed by WinXMorph software and it is shown in Fig. 3.

2.2 Solubility analysis

The solubility data is essential for growing good quality single crystals with bulk size in different temperature. Because, it gives the quantity of solute limit in a particular amount of solvent for a given temperature. The solubility of 2AP4N was determined for different temperatures from 35 to 50 °C with 100 mL of solvents such as water, acetone and methanol. These are taken separately in an airtight conical container. Initially, the constant temperature bath (CTB) was maintained at 35 °C with controlled accuracy of ± 0.01 °C and it was continuously stirred by an immersible motorized magnetic stirrer. The solubility was determined in the 100 mL of solvents (water, acetone and methanol) using the
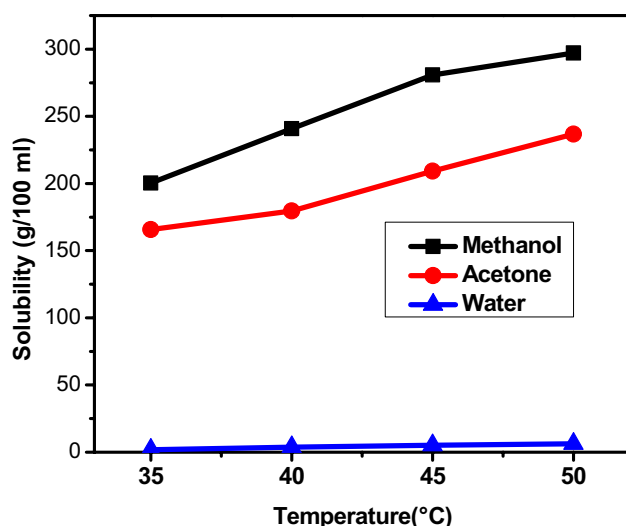
Fig. 4 Solubility curve of 2AP4N as a function of temperature

recrystallized material, which is slowly added to them. After reaching the saturation condition, the equilibrium concentration of the solution was analyzed by gravimetrical analysis. The same process was repeated several times to determine the solubility of 2AP4N material for different temperatures. The variation of solubility in different solvents with different temperatures is shown in Fig. 4.

3 Characterization studies

The optically good quality and defect free 2AP4N crystals were subjected to the various characterizations. The Bruker-kappa APEXII single crystal X-ray diffractometer (SXRD) with MoK$_\alpha$ ($\lambda = 0.71073$ Å) was used to measure the unit cell parameters of 2AP4N crystal. The powder XRD was carried out using BRUKER X-ray diffractometer with the CuK$_\alpha$ radiation ($\lambda = 1.5406$ Å). The optical quality of grown crystals was studied by Perkin-Elmer Lambda-35 UV–Vis NIR spectrophotometer in the region between 200 and 1100 nm. The functional groups of 2AP4N were recorded using Bruker AXS FTIR spectrometer in the region between 4000 and 500 cm^{-1} with transmission mode. Raman study was carried out by Bruker RFS 27 FT-Raman spectrometer in the range between 4000 and 50 cm^{-1} with resolution upto 2 cm^{-1}. The photoluminescence spectrum of 2AP4N was recorded using a Jobin Yvon (JY) make Fluorolog-FL3-11 spectrofluorometer with Xenon arc lamp (450 W) as the excitation source at room temperature. The thermogravimetric and differential thermal analysis (TG-DTA) was carried out between 30 and 370 °C at a heating rate of 10°C/min in the nitrogen atmosphere using a Perkin-Elmer Diamond instrument. The surface problems were identified using

COSLAB Model CMM-23 optical microscope in reflection mode. The Q-switched Nd:YAG nanosecond laser with input beam diameter of 8 mm operating in TM00 at 532 nm was used to measure LDT value of grown crystal. The Kurtz-Perry powder technique was used to measure the SHG efficiency of 2AP4N crystal using Nd: YAG laser 1064 nm.

3.1 Computational details

The 3D-Hirshfeld surfaces and 2D-fingerprint plots were generated using the Crystal Explorer 3.1 software. The frontier molecular orbital (FMO), Mulliken charges and molecular electrostatic potential (MEP) have been calculated for the 2AP4N molecule using DFT/B3LYP-6-311G (d,p) theory. The optimized geometrical parameters such as molecular energy, band gap, bond length, bond angle, dihedral angle and atomic charges were calculated using GAUSSIAN 09W package and the calculated values are visualized using Gauss View 5.0 program [15, 16]. The potential energy distribution (PED) for each vibrational mode was analyzed using VEDA4 (Vibrational energy distribution analysis) software [17]. Mercury 3.8 (using CIF file) was used to generate the crystal packing diagram of 2AP4N molecule. Gausssum 2.2 program [18] was used to calculate the group contributions to the molecular orbitals such as TDOS, PDOS and OPDOS.

4 Results and discussion

4.1 X-ray diffraction (XRD) analysis

2AP4N single crystal belongs to the orthorhombic crystal (space group Pna2$_1$) system and the calculated unit cell parameter values are a = 10.957 ($\pm$0.010) Å, b = 12.246 ($\pm$0.011) Å, c = 13.152 ($\pm$0.011) Å, $\alpha = \beta = \gamma = 90°$ and volume (V) = 1758 ($\pm$5) Å^3. The obtained unit cell parameters are in good agreement with the recent reported values [19, 20] and the values are given in Table 1. The powder X-Ray diffraction (PXRD) studies were carried out at room temperature in order to check the phase purity of materiel and its crystallinity. The obtained PXRD pattern for 2AP4N is in good agreement with that of CIF data and Rietveld refinement using the FullProf code [21]. The obtained peaks have been indexed and these are shown in

Table 1 Crystallographic data for 2AP4N crystal

Parameters	Present work	Reported [19]
Cell parameters	$a = 13.152$ Å, $b = 10.957$ Å, $c = 12.246$ Å; $\alpha = \beta = \gamma = 90°$	$a = 13.134$ Å, $b = 10.912$ Å, $c = 12.203$ Å; $\alpha = \beta = \gamma = 90°$
Space group	Pna2$_1$	Pna2$_1$
System	Orthorhombic	Orthorhombic

Fig. 5. It shows the well-defined refined peaks at specific 2θ angles and it shows a high degree of crystallinity of the grown 2AP4N single crystals.

4.2 Hirshfeld analysis

The Hirshfeld surfaces of the 2AP4N structure were analyzed to clarify the nature of the intermolecular interactions like hydrogen bond or van der Waals *(vdW)* contacts showing d_{norm}, d_e, d_i, *shape index and curvedness*. It is used to explore the strength and location of intermolecular interactions by mapping. The contribution to the electron density from the molecule under consideration is equal to the contribution from all other neighbouring molecules. For each point on that iso-surface, two distances are determined: (i) d_e is representing the distance from the point to the nearest nucleus external to the surface and (ii) d_i is representing the distance to the nearest nucleus internal to the surface. The normalized contact distance (d_{norm}) is based on both d_e and d_i and also the *vdW* radius of the appropriate internal (r_i^{vdw}) and external (r_e^{vdw}) atom of the surface.

$$d_{norm} = \frac{\left(d_i - r_i^{vdw} \right)}{r_i^{vdw}} + \frac{\left(d_e - r_e^{vdw} \right)}{r_e^{vdw}} \qquad (1)$$
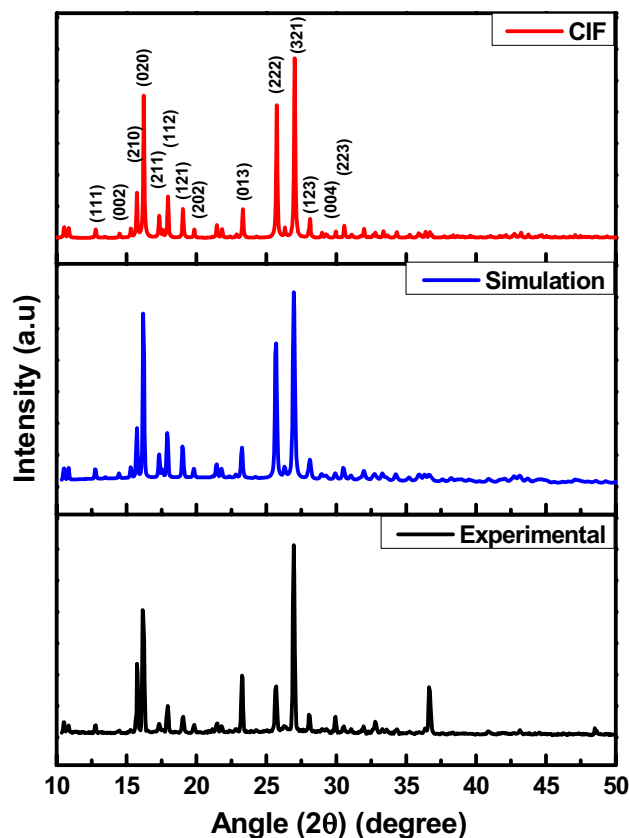

Fig. 5 Powder XRD patterns of 2AP4N crystal

The 3D-Hirshfeld surface and 2D-fingerprint plots were used to calculate the percentage of contribution by each intermolecular interaction of 2AP4N molecule. The 3D-Hirshfeld surface (d_{norm}) and 2D-fingerprint plots of 2AP4N molecule are shown in Fig. 6 and S. Figure 1 respectively. The d_i and d_e surface (Fig. 7a, b) indicates that the distance between the nearest nucleus internal and external [22] to the surface and the obtained values range from 0.63 to 2.44 Å and 0.63 to 2.18 Å respectively. The d_{norm} surface (Fig. 6) is a normalized contact distance [−0.76 Å (red) and 1.33 Å (blue)]. The color code red indicates short d_{norm} ranges and blue shows long ranges. The shape index surface (Fig. 7c) indicates the electron density surface shape around the molecular interaction (− 1 to 1 Å). The curvedness (Fig. 7d) indicates the electron density surface curves around the molecular interaction (− 4 to 0.44 Å). In the Hirshfeld surface, red regions indicate closer contact of molecules, the blue regions indicate farther contact of molecules and the white regions indicate the distance of contacts of molecules equal to the *vdW* separation. The percentage of various intermolecular contacts contributed to 2D fingerprint plots in 2AP4N molecule are shown in pie chart (Fig. 8) and it is given in Table 2. The analysis suggests that in the 2AP4N molecule hydrogen–hydrogen (H···H) contacts contribution is more (36.50%) when compared to other contacts in the same system. The oxygen–hydrogen (O···H) intermolecular interaction is 16.20% and it is the second highest interaction. The nitrogen–nitrogen (N···N) intermolecular interaction is found to be 0.10% and it is the lowest interaction in the present system. Other relative contributions of intermolecular interactions are H···O (14.60%), C···C (7%), C···H (6%),

Table 2 Contribution of intermolecular interaction of 2AP4N molecule

Intermolecular interaction	Contribution (%)
H–H	36.50
C–H	6.00
H–C	4.20
O–C	3.50
C–O	3.90
C–C	7.00
O–O	1.50
N–O	0.80
O–N	0.70
H–N	0.80
N–H	1.30
O–H	16.20
H–O	14.60
N–N	0.10
N–C	1.40
C–N	1.00

H···C (4.20%), C···O (3.90%), O···C (3.50%), C···O (2.5%). This result confirms 2AP4N molecule has supramolecular features.

4.3 Molecular geometry

The molecular geometry of the 2AP4N molecule with an atomic numbering scheme is shown in Fig. 9. The experimental data and optimized structural parameters such as bond length (Å), bond angle (°), and torsion angle (°) of 2AP4N are given in S. Table 1 (a), (b) and (c), respectively. When the electromagnetic radiation interacts with materials, it will get absorbed at the certain range of wavelength due to charge transfer. The present system consists of strong N–H···O intermolecular hydrogen bonding, which is caused by charge transfer. The two ring motifs nitrophenol and amino-pyrimidine molecules are connected and engaging in O–H···N and C–N=O, C–N–H bonds. These chains are leading to the formation of three dimensional (3D) network. Normally the dipolar molecules possessing an electron donor (D) and an electron acceptor (A) groups contribute to enhance the optical nonlinearity arising from the intramolecular charge transfer [23]. There are several intra and intermolecular close contacts in the present molecule such as O–H···N and C–N=O, C–N–H. The intramolecular interaction of 2AP4N molecules in different bond length (separated by 1–3 Å) is shown in S. Figure 2(a–c) and the intermolecular interaction (red color) is shown in S. Figure 2(d) at the maximum sum of *vdW* radii zero [24].

4.4 Vibrational analysis

Vibrational spectroscopy is an important tool for understanding the chemical bonding and to find out various functional groups present in a material. The FTIR and FT-Raman spectra results are shown in Figs. 10 and 11, respectively. In FTIR spectra, peaks at 3435 cm^{-1} and 3340 cm^{-1} represent asymmetric and symmetric stretching vibration of primary amine (NH$_2$) group respectively, which are absent in the FT-Raman spectrum. A peak at 3225 cm^{-1} is observed due to the intermolecular OH stretching vibration of (O–H···N) hydrogen bonding. The broadening of the peak is due to the presence of rich hydrogen bonds in the present crystal. The unresolved vibrations are clearly resolved at 3080 cm^{-1} in FT-Raman spectrum. The peak at 1666 cm^{-1} is due to the presence of N–H bending vibration, this vibration has not been observed in FT-Raman spectrum. The ring carbon–carbon (C–C) stretching vibrations occur in the region between 1625 and 1430 cm^{-1}. The peak at 1617 cm^{-1} indicates stretching vibration of C=C in aromatic and it is not present in FT-Raman. The peak at 1479 cm^{-1} is the asymmetric stretching vibration of aromatic (N–O) nitro group. The skeletal vibration of benzene ring usually is at 1501 cm^{-1}. The 1550–1680 cm^{-1} regions in the FT-Raman

spectra of the complexes contain the phenyl C=C stretching mode. The peak at 1589 cm^{-1} represents the aromatic stretching vibration. The peak at 1330 cm^{-1} is due to the N=O strong symmetric stretching vibration of aromatic nitro group and it is present in FT-Raman spectrum at 1327 cm^{-1} [25]. The peak at 1286 cm^{-1} is assigned to strong C-N stretching vibration of aromatic amine and also it is present in FT Raman spectrum at 1297 cm^{-1}. The intense peaks at 1107 cm^{-1} and 1105 cm^{-1} observed at IR and Raman spectra respectively are due to the C–N stretching vibrations. The peak at 953 cm^{-1} is assigned to C–H out of plane bending vibrations. Also the band around 1000 cm^{-1} is attributed to very weak skeleton vibration of aromatic carbons [26]. Peak at 845 cm^{-1} is the N–H out-of-plane bending absorption. The band due to the C–N stretching vibration is of weak-to-medium intensity and occurs at 920–850 cm^{-1}. The C–H out-of-plane deformation band is at 865 cm^{-1}. In and out-of-plane bending of C–H showed their peaks at 754 cm^{-1} and 694 cm^{-1}. In a FT-Raman spectrum, the very weak signal at 754 cm^{-1} indicates C-H vibration. The FTIR spectrum has peak at 635 cm^{-1} which represents NO$_2$ scissoring [27]. Normally, nitro group contains organic compounds which exhibits a very strong band at 655–605 cm^{-1} due to the deformational vibration of the NO$_2$ group and their corresponding FT-Raman peak appeared at 636 cm^{-1}. The peak at 543 cm^{-1} is the out of plane bending vibration of C=O.

4.5 UV–Vis NIR analysis

The optical transmittance is an important characteristic of an NLO material. Hence the transmittance spectrum of 2AP4N single crystal was recorded on the (001) plane with a sample of thickness 2 mm. The transmittance spectra of 2AP4N single crystal is shown in Fig. 12. From this spectrum, grown crystal has good optical transmission in the visible and near IR regions. The higher transmittance of the grown crystal may be attributed to a less surface scattering, line and point defects, etc [28]. The fundamental UV–Visible cut-off wavelength for 2AP4N crystal was found to be at 470 nm. The optical absorption co-efficient (α) can be calculated using the following relation.

$$\alpha = \frac{2.3026}{t} \log_{10}\left(\frac{100}{T}\right) \tag{2}$$

where T is the transmittance (%) of different wavelengths, t is the thickness of the sample (2 mm). The dependence of α with the corresponding photon energy $(h\upsilon)$ helps to study the band structure and the type of electronic transition. The optical band gap can be described by the Tauc's plot relation [29].

$$(\alpha h\upsilon) = A\left(h\upsilon - E_g\right)^m \tag{3}$$

where α is the linear absorption co-efficient, $h\upsilon$ is photon energy, E_g is the optical band gap energy, A is a constant and m is the characteristics of electronic transition. Normally the electron transition from valence band (lower energy states) to conduction band (excited energy states), which may be either direct or indirect and also both possess forbidden transitions when absorbing incident photons. These effects are considered in terms of numerical values. These are considered as electronic transition numbers (m) such as 1/2 for direct allowed transition, 2 for indirect allowed transition, 3/2 for direct forbidden transition and 3 for indirect forbidden transition. Further, we have to determine the value of m and it indicates the type of electronic transition of 2AP4N single crystal. Taking logarithm on both sides and differentiating the Eq. (3) with respect to $h\upsilon$, we get the following form [30].

$$\ln(\alpha h\upsilon) = \ln(A) + m\ln\left(h\upsilon - E_g\right) \qquad (4)$$

$$\frac{d[\ln(\alpha h\upsilon)]}{d(h\upsilon)} = \frac{m}{\left(h\upsilon - E_g\right)} \qquad (5)$$

The quantity E_g can be determined from a graph plotted between $(ln\,(\alpha h\upsilon))/h\upsilon$ and $h\upsilon$ which is shown in Fig. 13a. From this figure, the discontinuity in line gives the information about electronic transitions of 2AP4N single crystal. The sharp discontinuity line at a particular maximum energy is called as knee point, which was found to be 2.64 eV. The value of m was obtained from the graph plotted between $(\ln(\alpha h\upsilon))$ and $\ln(h\upsilon - E_g)$. The value of m was found to be $0.43 = 0.5 = 1/2$ for the grown crystal by extrapolating linear fit as shown in Fig. 13b, which is approximately equal to the 0.5 (1/2). This is the evidence for the fact that the electronic transition of 2AP4N crystal is allowed for direct band gap nature. The Tauc's plot relation has been modified as given below for direct allowed transition.

$$(\alpha h\upsilon) = A\left(h\upsilon - E_g\right)^{\frac{1}{2}} \qquad (6)$$

A graph is plotted between photon energy $(h\upsilon)$ and $(\alpha h\upsilon)^2$ and the band gap is obtained by extrapolating the linear portion of the curve to $\alpha = 0$ as shown in Fig. 13c. The band gap of the grown 2AP4N crystal is found to be 2.55 eV, this band gap energy was theoretically confirmed by Frontier molecular orbital (FMO) analysis, which is given in the following section.

4.6 Frontier molecular orbital (FMO) analysis

The HOMO–LUMO energy gap (ΔE) reflects the chemical activity of the molecule which confirms the interaction of charge transfer within the 2AP4N moiety and it has also an important role in electrical and optical properties and chemical reactions. The HOMO and LUMO are also called as frontier molecular orbitals (FMO). It gives the information about the transition of the electron from the ground state to first excited state. It is described by one electron excitation for the HOMO to LUMO level. The FMO is composed of the π-atomic orbital and it is derived from π–π* electronic transition [31]. The molecular energies of HOMO and LUMO were calculated for the 2AP4N molecule and the values are -6.01 and -3.21 eV, respectively. These are shown in Fig. 14. In this figure, red and green colors represent the positive and negative charge distribution region. The difference (ΔE) between HOMO and LUMO was found to be 2.79 eV, which indicates the band gap energy of 2AP4N molecule. The theoretically obtained value of ΔE (2.79 eV) is nearly equal to the band gap (2.55 eV) obtained from the experimental technique (Fig. 9c).

The energy gap between HOMO and LUMO is a critical parameter to determine molecular electrical transport properties. The global chemical reactivity descriptors of molecules such as hardness (η), chemical potential (μ), softness (S) and electronegativity (χ) can be calculated using the following equations [32, 33]:

$$\eta = \frac{(I-A)}{2}; \mu = \frac{-(I+A)}{2}; S = \frac{1}{2\eta} \text{ and } \chi = \frac{(I+A)}{2} \qquad (7)$$

where I and A are the ionization potential and electron affinity of the molecules respectively. The ionization energy $(I = -E_{HOMO})$ and electron affinity $(A = -E_{LUMO})$ can be expressed through HOMO and LUMO orbital. It is widely known that the chemical hardness and softness are useful properties to measure the molecular stability and reactivity. The electrophilicity index (ω) is a measure of energy lowering due to the maximum electron flow between donor and acceptor [34]. It has been obtained from the following equation:

$$\omega = \frac{\mu^2}{2\eta} \qquad (8)$$

The maximum amount of charge transfer (ΔN_{max}) in the direction of the electrophile is predicted, which describes the tendency of the molecule to acquire an additional electronic charge from the environment. The maximum amount of electrophilic system is given in the following equation [35]:

$$\nabla N_{\max} = -\frac{\mu}{\eta} \qquad (9)$$

The two reactivity indices quantify the nucleophilic and electrophilic capabilities. The nucleofugality (ΔE_n) and electrofugality (ΔE_e) are defined as follows:

$$\nabla E_n = EA + \omega = \frac{(\mu + \eta)^2}{2\eta} \qquad (10)$$

$$\nabla E_e = IP + \omega = \frac{(\mu - \eta)^2}{2\eta} \tag{11}$$

The calculated values are: chemical hardness $(\eta) = 1.39$ eV, reciprocal of hardness $(S) = 0.35$ eV, chemical potential $(\mu) = -4.61$ eV, electronegativity $(\chi) = 4.61$ eV, global electrophilicity index $(\omega) = 7.61$ eV, nucleofugality $(\Delta E_n) = 3.69$ eV, electrofugality $(\Delta E_e) = 12.92$ eV and maximum charge transfer $\Delta N_{max} = 3.30$ eV.

4.7 Total, partial and overlap population-density of states (DOS)

The density of states (DOS) of a system describes the number of states per interval of energy at each energy level that is available to be occupied by electrons. Consideration of the HOMO and LUMO energy may not yield a realistic description of the frontier orbitals. For this reason, the total density of states (TDOS), partial density of states (PDOS), and overlap population density of states (OPDOS) or Crystal Orbital Overlap Population (COOP) density of states are required [36]. The DOS spectrum was formed by convoluting the molecular orbital information with Gaussian curves of unit height [full width at half maximum (FWHM) is 0.3 eV] using the Gauss-Sum 2.2 program [37]. The calculated TDOS of 2AP4N is shown in Fig. 15. The calculated PDOS and OPDOS are shown in S. Figures 3 and 4, respectively. The green and red lines in the TDOS spectrum indicate the occupied orbitals (HOMO levels) and virtual orbitals (LUMO levels), respectively. The total, partial, and overlap population density-of-states provides a pictorial representation of molecule orbital compositions and their contributions to the chemical bonding. A positive overlap population of the OPDOS indicates a bonding interaction, negative overlap population of the OPDOS indicates an anti-bonding interaction and zero value indicates non-bonding interactions [18, 38]. The partial density of states (PDOS) presents the composition of the fragment orbitals contributing to the molecular orbitals (S. Fig. 3). From the COOP or OPDOS diagram (S. Fig. 4), one observes the overlap between hydrogen with carbon (blue line), hydrogen with nitrogen (green line), hydrogen with oxygen (red line), carbon with nitrogen (violet line), carbon with oxygen (pink line) and nitrogen with oxygen (yellow line). In general overlap of carbon and nitrogen atoms with the ring atoms exhibit antibonding interaction. Also overlap of hydrogen atoms with ring atoms indicates the positive interaction. From the OPDOS plots, it can be calculated that the 2AP4N has anti-bonding character in the HOMO and LUMO molecular orbitals.

4.8 Mulliken charge analysis

Mulliken atomic charge calculations have a significant role in the application of quantum chemical calculations to the molecular system because the atomic charges affect the electronic structure, dipole moment, molecular polarizability and other properties in molecular systems. It is generally accepted that atomic charges yielded by Mulliken population are basis set dependent [39]. The total atomic charges of 2AP4N molecule are obtained from the Mulliken charge population using DFT method. Atomic charges play an important role in quantum chemistry. Mulliken atomic charge population is one of the simplest pictures of charge distribution and it predicts the net atomic charges in the molecule [40]. The Mulliken atomic charge distribution and plots of Mulliken atomic charges of all the atoms are shown in Figs. 16 and 17, respectively. The atomic charges of the molecule are ranging from 0.5 to -0.6 (e) (Fig. 17) and the color codes such as black, red, blue and orange indicate N, C, H and O atoms respectively. The highest value is observed in C3 ($+0.456$) and O30 (-0.585), whereas the lowest value is observed in C21 (-0.005) and C23 (-0.015) atom. Almost all the hydrogen atoms exhibit positive charge and all the oxygen atoms exhibit negative charge. The carbon and nitrogen atoms possess both positive and negative charges. The carbon (C3, C5, C7, C19, C22, C34 and C37) atoms exhibit positive and the other carbon atoms (C4, C6, C35, C36, C38 and C39) exhibit negative charges. The sum of Mulliken atomic charges for 2AP4N molecule becomes zero and thus maintains the charge neutrality.

4.9 Molecular electrostatic potential (MEP) analysis

The molecular electrostatic potential (MEP) surface map is used to visualize the charge distribution of 2AP4N molecules and to analyse the charge related properties such as electrophilic, nucleophilic reactions and hydrogen bonding interactions. The electrostatic potential is mapped onto the constant electron density surface. The MEP is super-imposed on top of the total energy density as a shell. It is a useful feature to study the reactivity of electrophile and it will be attracted to negative regions (where the electron distribution effect is dominant). In the majority of MEPs, the maximum negative region which preferred site for electrophilic attack is indicated by red color and the maximum positive region which preferred site for nucleophilic attack is indicated by blue color. The negative electrostatic potential emerged due to the attraction of the proton by the electron density (ED) cloud and the positive electrostatic potential commenced due to the repulsion of the proton by the nuclei [32, 33]. MEP displays the size and shape of a molecule. It is given in terms of color grading (Fig. 18). The importance of MEPs lies in the fact that it simultaneously displays the molecular size,

shape, as well as positive regions in terms of color grading and it is very useful in research of molecular structure with its physicochemical relationship [41]. In general, the electrostatic potential increases in the following manner: Red < Orange < Yellow < Green < Blue [34, 42]. The electron distribution occurs in the range from $-9.47\,E^{-2}$ (deepest red) to $9.47\,E^{-2}$ (deepest blue). The color scheme for the MEP surface is blue color (positive) and it indicates the nucleophilic attack as well as strongest attraction, red color (negative) shows the electrophilic attack as well as strongest repulsion, light blue for the slightly electron deficient region and yellow for the slightly electron-rich region [43]. The negative potential site is localized mainly around the oxygen atom which is associated with electrophilic reactivity. All the hydrogen and nitrogen (carbon-attached) atoms are of positive potential and this is associated with nucleophilic reactivity of the 2AP4N molecules, remaining to be neutral particles that means zero potential. The contour map of total electrostatic potential of 2AP4N has been constructed by the DFT method and it is shown in Fig. 19. It confirms the various negative and positive potential sites of the molecule in accordance with the total electron density surface.

4.10 Natural bonding orbital (NBO) analysis

The NBO analysis provides an efficient method for studying intra and intermolecular bonding interactions among the bonds and it also provides a convenient basis for investigating charge transfer or conjugative interaction in the molecular system [44, 45]. It gives the information about interactions of both filled and virtual orbital spaces, which can enhance the analysis of intra-inter molecular interactions. It was carried out to evaluate the donor–acceptor interactions in the NBO basis. The interaction results in a loss of occupancy from the localized NBO of the idealized Lewis structure into an empty non-Lewis orbital. The donor (i) and acceptor (j) the stabilization energy ($E^{(2)}$) associated with the delocalization ($i \rightarrow j$) is determined as

$$E^{(2)} = \Delta E_{ij} = q_i \frac{F_{ij}^{\,2}}{E_j - E_i} \qquad (12)$$

where q_i is the donor orbital occupancy, E_i, E_j are diagonal elements (orbital energies) and F_{ij} is the off-diagonal NBO Fock matrix element. In the larger $E^{(2)}$ value, the interaction between the electron donors and acceptors moieties is more intensive. The NBO analysis allows the estimating energy of the molecule with the same geometry in the absence of electronic delocalization. The intramolecular N–H···O hydrogen bonding is formed by the orbital overlap between n(O) and σ*(N–H), causing stabilization of H-bond in the systems and that leads to intramolecular

charge transfer (ICT). This interaction results in increased electron density (ED) of the N–H antibonding orbital, strengthens the N–H bond [46]. The orbital overlap between a lone pair $n_1(N_2)$ and σ*(N_1–C_3) antibonding orbital with stabilization energy of 84.47 kcal/mol was obtained for 2AP4N molecule. Most important interactions in the 2AP4N molecule with the high $E^{(2)}$ values are $n_1(N_2) \rightarrow$ σ*(N_1-C_3), σ*(N_1–C_3) $\rightarrow$ σ*(C_4–C_5), σ*(N_1–C_3) $\rightarrow$ σ*(C_6–C_7), σ(C_6–C_7)$\rightarrow$σ*(C_4–C_5),σ(C_4–C_5)$\rightarrow$σ*(N_1–C_3),σ(C_4–C_5)$\rightarrow$σ*(C_6–C_7) and π (N_1–C_3) $\rightarrow$ π*(C_6–C_7) with energy values of 84.47, 55.66, 29.52, 19.54, 34.26, 12.95 and 22.13 kcal/mol, respectively. This high energy values lead to ICT interactions in the molecule [47, 48]. In NBO analysis large $E^{(2)}$ value shows the intensive interaction between the electron donors and the electron-acceptors and greater extent of conjugation of the whole system. The possible intensive interactions are given in S. Table. 2.

4.11 First order hyperpolarizability analysis

Nowadays DFT studies become one of the inexpensive and effective tools to design the second order NLO materials. Also, it gives the useful information regarding the relationship between the molecular structure and NLO properties. To understand the microscopic origin of nonlinear behaviour of the molecule (2AP4N), the dipole moment (μ), polarizability (α) and first-order hyperpolarizability (β) tensor [49] have been executed by B3LYP/6-311G(d,p) basis set using Gaussian 09w program. When a molecule with permanent electric dipole moment ($\mu_e\,(0)$) interacts with an external constant electrostatic field (E), the change in the dipole moment can be written as:

$$\mu_{total} = \mu_0 + \alpha_{ij}E_j + \beta_{ijk}E_{ijk}E_jE_k + \dots \qquad (13)$$

where α is the linear polarizability, $\mu_e\,(0)$ is the permanent dipole moment and β_{ijk} is the hyperpolarizability tensor components. The total dipole moment is defined as [50]:

$$\mu = \left(\mu_x^2 + \mu_y^2 + \mu_z^2 \right)^{\frac{1}{2}} \qquad (14)$$

where, μ_x, μ_y, and μ_z are dipole moments along x, y and z directions. The total linear polarizability (α_{total}) can be calculated by the following equation:

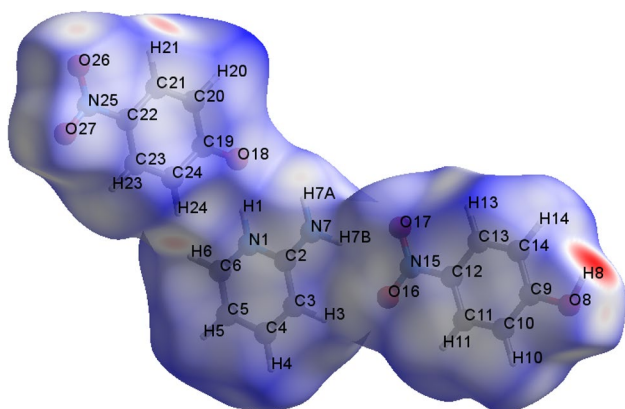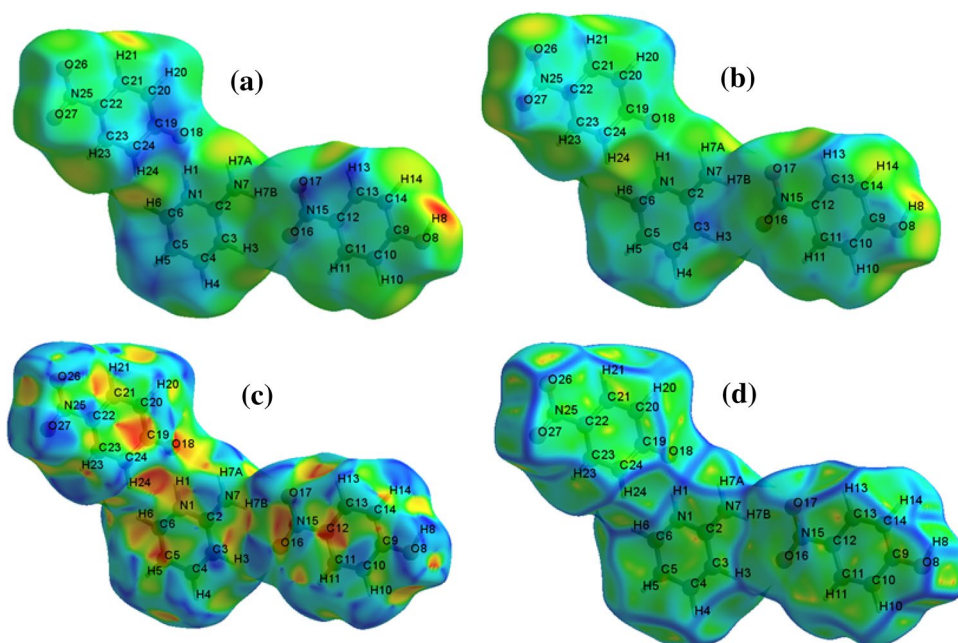$$\alpha_{total} = \frac{\left(\alpha_{xx} + \alpha_{yy} + \alpha_{zzx} \right)}{3} \qquad (15)$$

where, α_{xx}, α_{yy} and α_{zz} are the diagonal components of polarizability tensor. The anisotropy of the polarizability ($\Delta\alpha$) can be calculated by the following expression:

$$\nabla\alpha = \frac{1}{\sqrt{2}} \left(\left(\alpha_{xx} - \alpha_{yy} \right)^2 + \left(\alpha_{yy} - \alpha_{zz} \right)^2 + \left(\alpha_{zz} - \alpha_{xx} \right)^2 + 6\alpha_{xx}^2 \right)^{\frac{1}{2}} \qquad (16)$$

Table 3 NLO properties of 2AP4N calculated using DFT at B3LYP/6-311G (d,p) level

Dipole moment (debye)		Polarizability		First hyperpolarizability	
μ_x	− 22.35	α_{xx}	− 199.59 (a.u.)	β_{xxx}	− 1196.61 (a.u.)
μ_y	7.88	α_{yy}	− 124.10 (a.u.)	β_{yyy}	96.16 (a.u.)
μz	− 0.21	α_{zz}	− 162.84 (a.u.)	β_{zzz}	− 0.29 (a.u.)
$\mu Total$	23.70	α_{Total}	2.40×10^{-23} (esu)	β_{xyy}	− 137.88 (a.u.)
		$\Delta\alpha$	5.21×10^{-23} (esu)	β_{xxy}	87.23 (a.u.)
				β_{xxz}	− 148.98 (a.u.)
				β_{xzz}	− 68.56 (a.u.)
				β_{yzz}	4.56 (a.u.)
				β_{yyz}	− 2.24 (a.u.)
				β_{xyz}	16.14 (a.u.)
				β_{Total}	1.07×10^{-23} (esu)

Fig. 6 3D-Hirshfeld surface (d_{norm}) of 2AP4N molecule

The first order hyper-polarizability is a third rank tensor which can be depicted by a $3 \times 3 \times 3$ matrix. Due to the Kleinmann symmetry [51], the 27 components of the 3D matrix can be minimized to 10 components. Using the DFT calculations, 10 components of this matrix such as β_{xxx}, β_{xxy}, β_{xyy}, β_{yyy}, β_{xxz}, β_{xyz}, β_{yyz}, β_{xzz}, β_{yzz} and β_{zzz} have been obtained. Using the x, y and z components, one can calculate the magnitude of the total first-order hyperpolarizability (β_{total}) tensor by the following equations [52]:

$$\beta_{total} = \left(\beta_x^2 + \beta_y^2 + \beta_z^2 \right)^{\frac{1}{2}} \tag{17}$$

$$\beta_x = \beta_{xxx} + \beta_{xxy} + \beta_{xxz}, \beta_y = \beta_{yyy} + \beta_{yyz} + \beta_{xyy}, \beta_z = \beta_{zzz} + \beta_{xzz} + \beta_{yzz} \tag{18}$$

The calculated total electric dipole moment (μ) = 23.70 Debye, total polarizability (α_{total}) = 2.40×10^{-23} esu, the anisotropy of the polarizability ($\Delta\alpha$) = 5.21×10^{-23} esu and first-order hyperpolarizability (β_{total}) = 1.071^{-29} esu are given in Table 3. The values of α and β in atomic units (a.u.) have been converted into electrostatic unit (esu) (α: 1 a.u. = 0.1482×10^{-24} esu; β: 1 a.u. = 8.47×10^{-33} esu). The first-order hyperpolarizability value of urea molecule is compared with 2AP4N molecule. The β_{2AP4N} is 28.6 times greater than that of urea molecule (β_{Total} of urea is 0.372×10^{-30} esu). The high β value and non-zero value of dipole moment (μ) indicates that the title compound may be a suitable candidate for NLO applications.

Fig. 7 **a** di, **b** de, **c** shape index and **d** curvedness surface of 2AP4N molecule
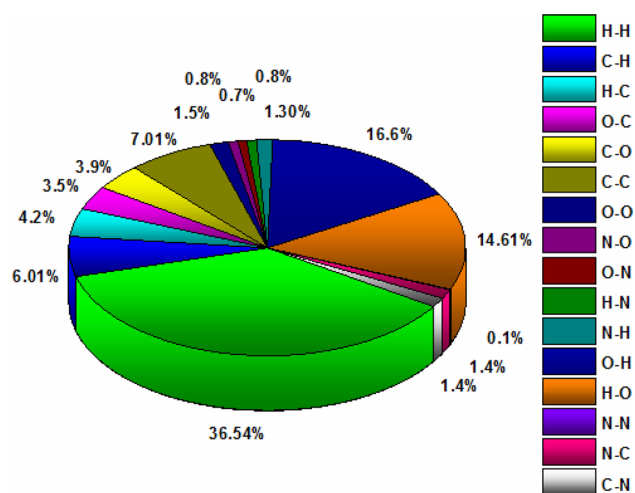
Fig. 8 2D fingerprint plots of 2AP4N molecule in a pie chart
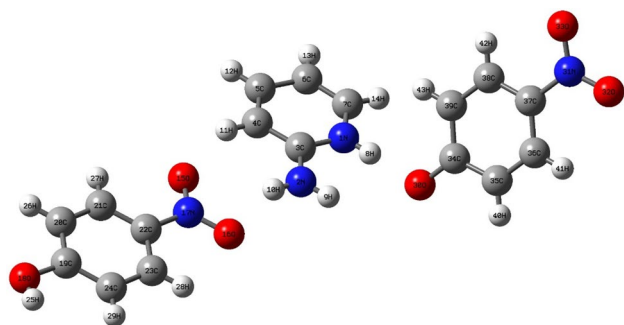
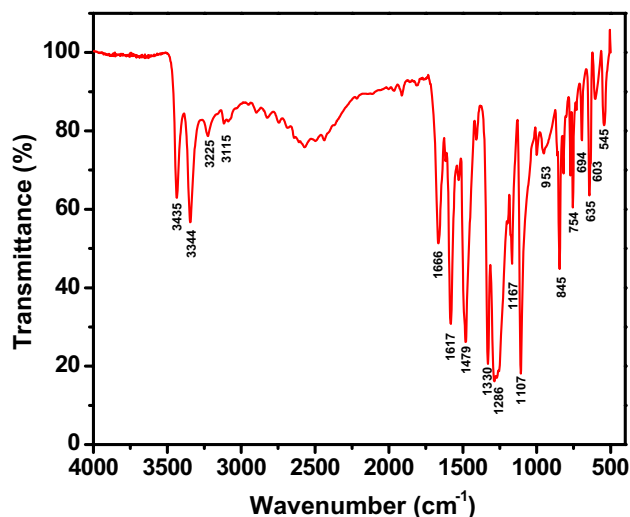

Fig. 9 Atomic numbering scheme of 2AP4N
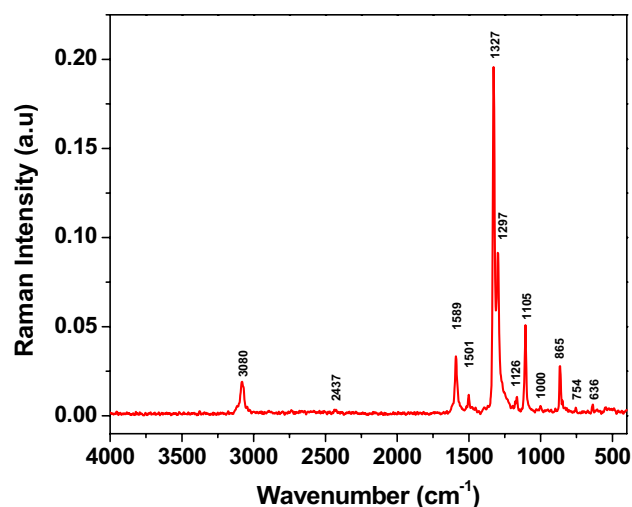

Fig. 10 FTIR spectrum of 2AP4N crystal
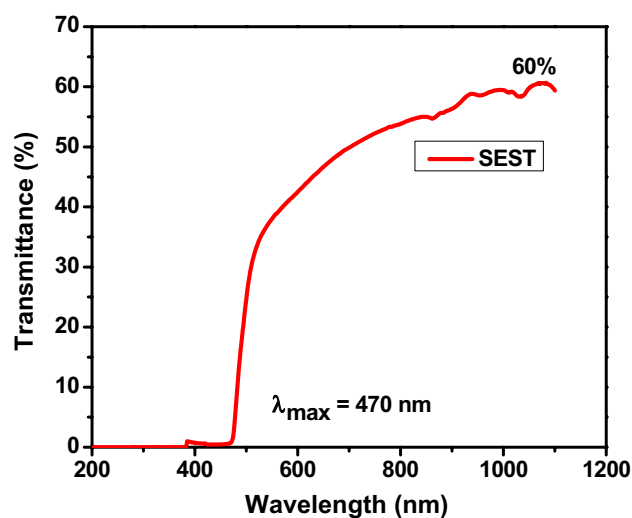

Fig. 11 FT-Raman spectrum of 2AP4N crystal

Fig. 12 UV–Vis NIR spectrum of 2AP4N single crystal

4.12 Photoluminescence (PL) studies

The photoluminescence (PL) is one of the effective tools to provide relatively direct information about the physical properties of materials at the molecular level. In order to identify the photoluminescence characteristics of 2AP4N crystal, the PL study was recorded at room temperature. The sample was excited with the 400 nm wavelength. The emission spectrum was recorded in the wavelength ranging from 450 to 700 nm. Excitation and emission wavelengths were obtained by changing the excitation wavelength under a fixed emission wavelength and vice versa. The photoluminescence spectrum of the grown 2AP4N single crystal is shown in Fig. 20. Fluorescence is the spontaneous emission of light radiation during the transition of
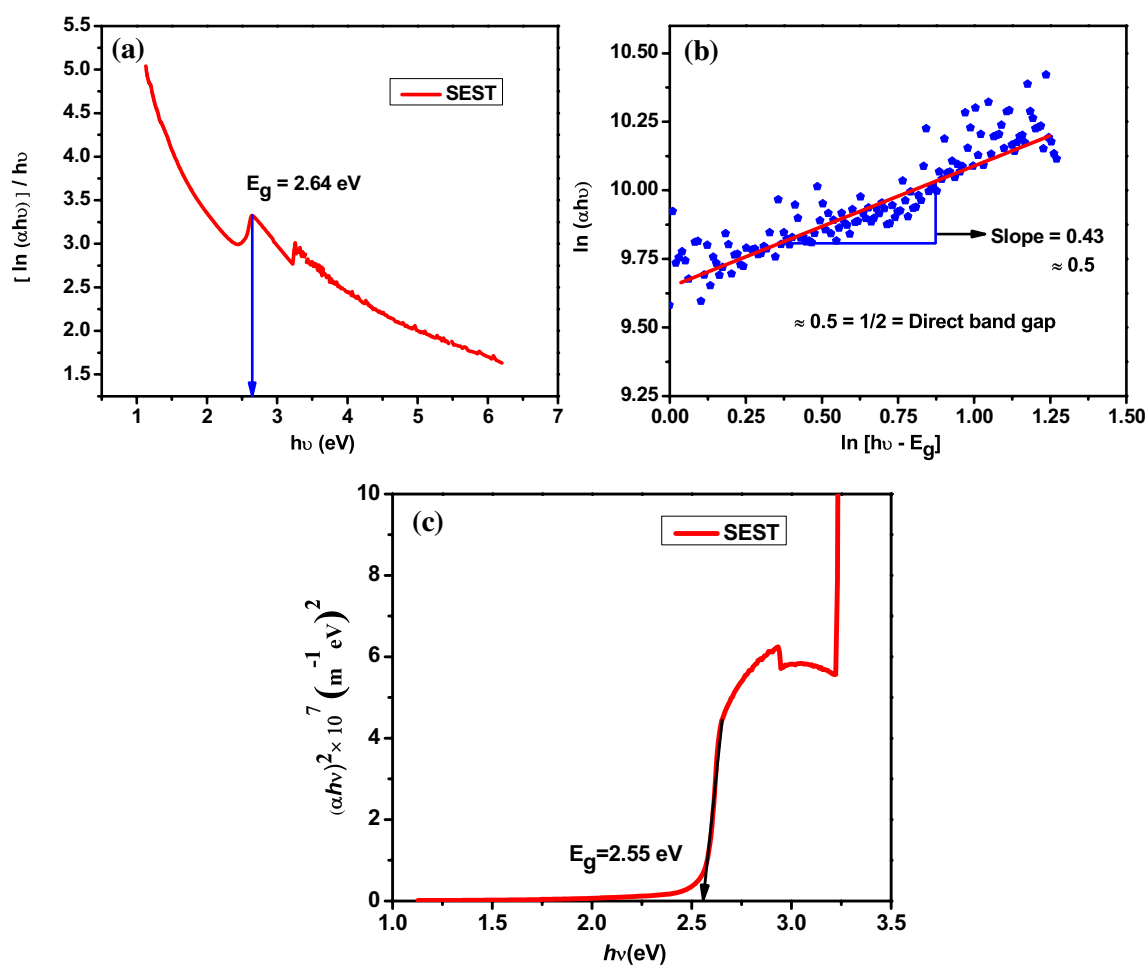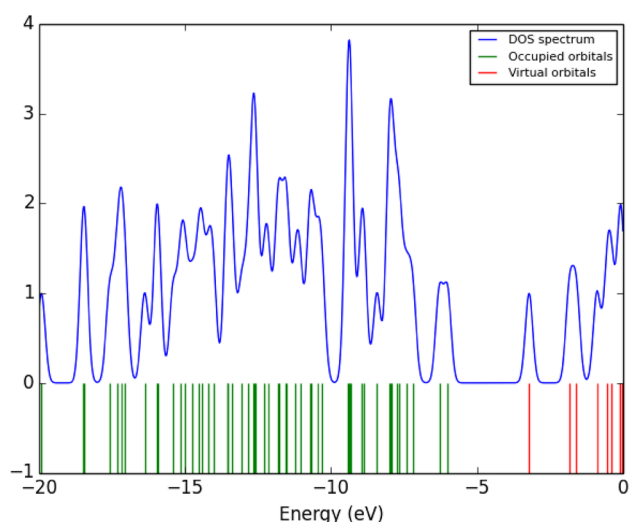
Fig. 13 **a** Graph plotted between $(ln\,(\alpha h\upsilon))/h\upsilon$ and $h\upsilon$, **b** graph between $(ln(\alpha h\upsilon))$ and $ln(h\upsilon - E_g)$, **c** graph between $(h\upsilon)$ and $(\alpha h\upsilon)^2$
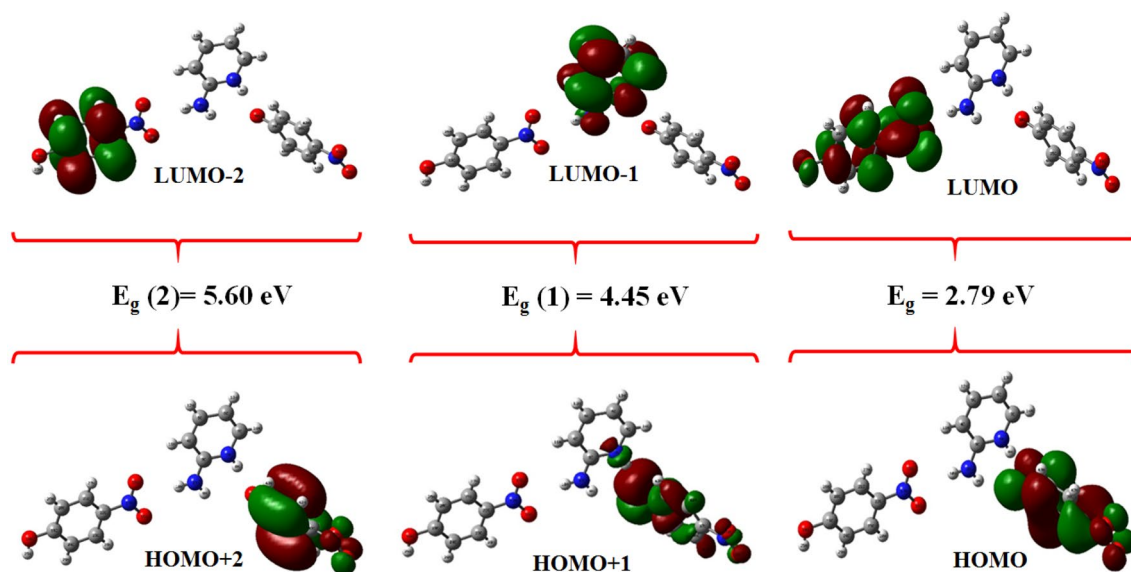
Fig. 14 HOMO–LUMO diagram of 2AP4N

Fig. 15 Total electronic density of states (TDOS) of 2AP4N molecule

Fig. 17 Mulliken atomic charges of all the atoms

the system from its lowest vibrational energy level of first excited state (S_1) back to its ground state (S_0). The energy states of T_1 represent the first level triplet electronic transition [53]. The loss of photons emission is due to the vibrational relaxation, internal conversion and intersystem crossing. The Jablonski energy diagram illustrating the energy transitions between different electronic states is shown in Fig. 21. Aromatic molecules which contain multiple conjugated bonds (π bonds of sp^2 hybrid orbitals) possess a high degree of resonance stability. The 2AP4N crystal consists of phenoxy ion (benzene derivative) having delocalized π-electrons in carbon bonds [54]. Small intense emission peaks were observed at 470 nm (2.63 eV) and 482 nm (2.57 eV). A sharp high intense emission peak is obtained at 500 nm (2.4 eV) and this may be due to charge transfer between the pyridine and hydroxyl group. This emission of transition occurs from the excited state
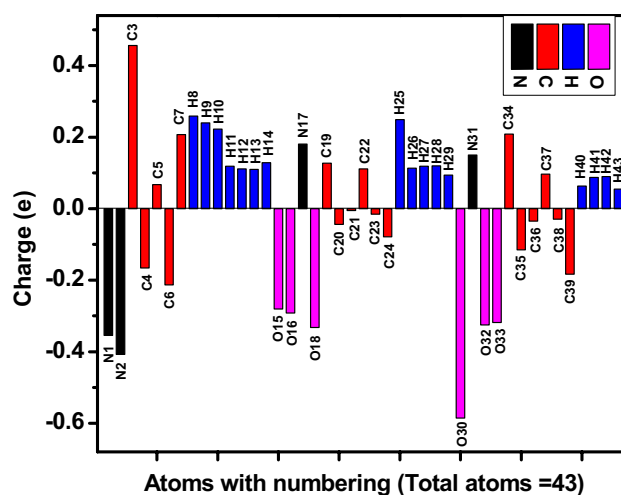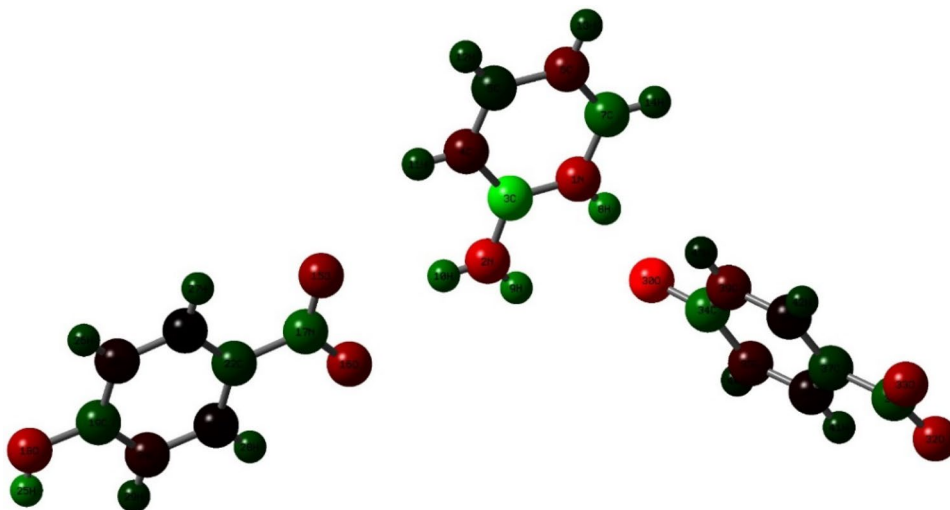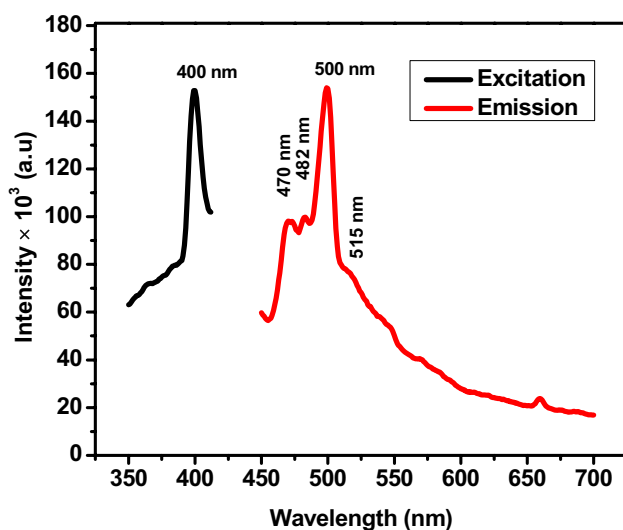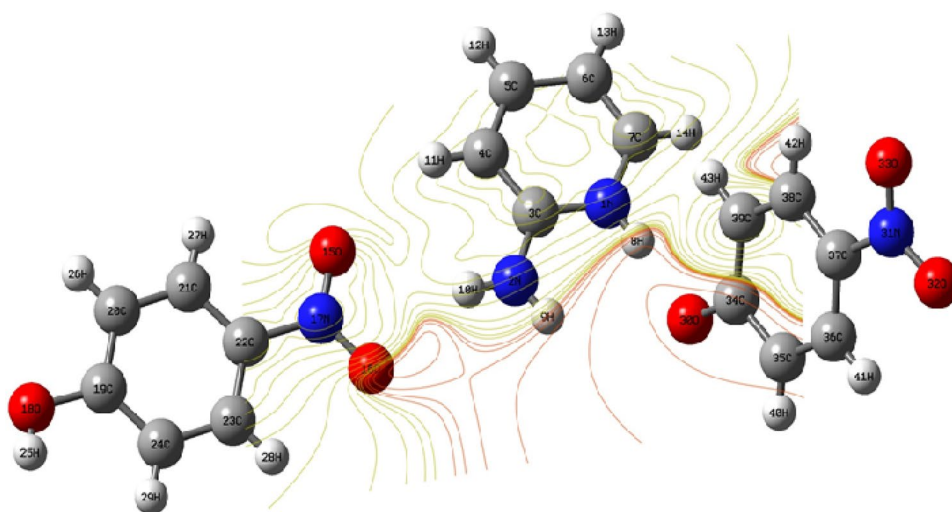

Fig. 18 Total density molecular electrostatic potential (MEP) of 2AP4N

Fig. 16 Mulliken atomic charge distribution

Fig. 19 The contour map of total density electrostatic potential of 2AP4N

Fig. 20 The photoluminescence (PL) spectrum of the grown 2AP4N
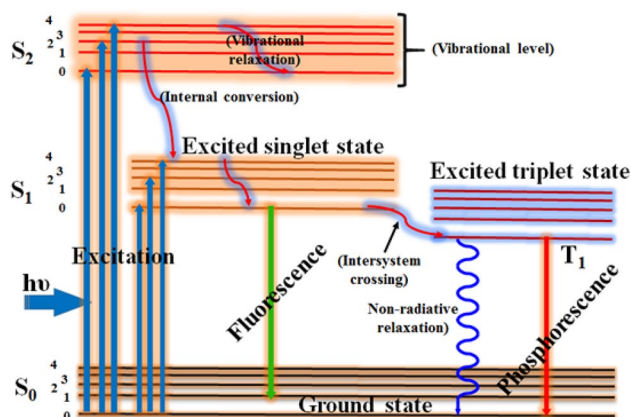
Fig. 21 Jablonski energy diagram

S_{1-0} to the ground state S_{0-1}. The broad emission peak is observed from 515 nm (2.33 eV) to 650 nm (1.90). This may be due to the vibrations in the crystal lattices [55]. These vibrations are caused by thermal vibrations of atoms due to temperature changes and also other reasons such as vibrational relaxation, internal conversion and intersystem crossing may occur during the excitation. Moreover, the emission peaks are broad and asymmetric. This behaviour indicates the existence of several transitions levels below the conduction band or may be due to the overlap of various emission peaks from these levels. This is associated with the presence of defects inside the band gap, probably due to the vacancies or dislocations in a grown crystal. But intensity of the peak depends upon the crystallinity. Hence it can be useful for fluorescence detection in the visible range and LED applications [55].

4.13 TG/DTA analysis

Thermogravimetric and differential thermal analysis (TG-DTA) was carried out to confirm the thermal behaviour of 2AP4N crystal. The crystalline sample of weight 3 mg was taken in alumina crucible. Nitrogen gas was continuously allowed inside the furnace for maintaining inert atmosphere around the sample. The sample was heated in the range from 30 to 250 °C with the heating rate of 10 °C/min. The TG-DTA graph is shown in Fig. 22. From the TGA curve, it has been observed that the weight loss started at 115 °C due to degradation of 2AP4N crystal. There was no remarkable weight loss observed between 30 to 115 °C and it confirms the absence of adsorbed water molecules. But there was a sharp endothermic peak starting at 90 °C, the melting point of 2AP4N crystal and it was completed at 95 °C. The 2AP4N crystal exhibits a single stage decomposition and it starts around 115–220 °C with a mass loss of almost 98% of the material. This major decomposition is may be due to
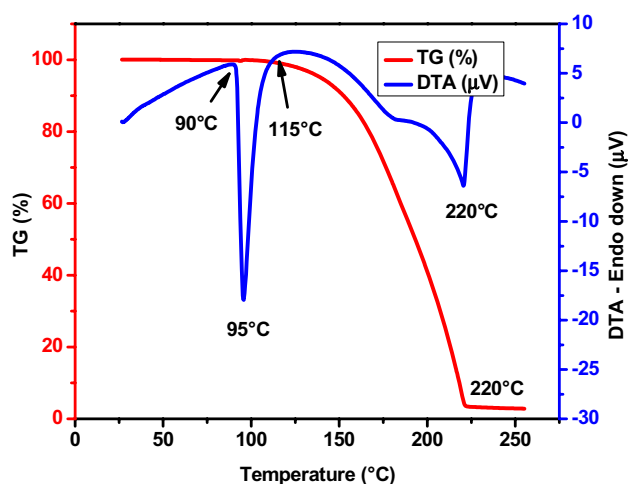
Fig. 22 TG-DTA analysis of 2AP4N single crystal

liberation of some volatile products [56] and remaining 2% may be the residual carbons. In the present case, there is no weight loss when temperature is increased upto 90 °C. The grown 2AP4N crystal was thermally stable upto 90 °C.

4.14 Chemical etching analysis

The chemical etching analysis was carried out to determine the dislocation distributions and surface features of the grown 2AP4N single crystals. The optically good quality 2AP4N crystal was chosen. (001) plane was used and it was soaked in Millipore water as an etchant. The surface of the grown 2AP4N crystal was analyzed by an optical microscope. Well-defined elongated sharp cone-shaped etch pits have been obtained with the 5 s etching time. Randomly distributed and strictly oriented etch pits were seen. The as grown crystal surface and etched surfaces are shown in Fig. 23a and b respectively. The 170 ($\pm$5) pits were observed per 25×10^{-4} cm². Therefore the etch pit density (EPD) was found to be 6.80×10^4 cm^{-2} for the grown crystal. There is no solvent inclusion, grain boundaries and micro-cracks which clearly confirms that the grown 2AP4N crystal has less dislocations.

4.15 Laser-induced damage threshold (LDT) studies

When the material goes for NLO applications, it must have ability to withstand high power laser intensities. Hence, the high optical surface damage tolerance materials are extremely important in the performance of nonlinear optical (NLO) and optoelectronic device applications. The laser damage threshold (LDT) of the NLO components depends on physical and chemical imperfections particularly on growth dislocations [57]. If the grown crystal contains more dislocations, it results in low damage threshold as these dislocations influence to reduce the strength of interatomic bonds of the material. In the present work, 5 mm thick 2AP4N crystal was used. The output laser power was controlled by an attenuator (combination of half-wave plate and Brewster's polarizer) and the crystal was placed at the focal point using translation (X–Y) stage. The laser energy was recorded by a digital power meter. The input laser energy was increased until the sample gets damaged. When the laser irradiation increases, the sample causes localized heating due to the absorptions and then it gets to vaporization, melting locally as well as fracture may be possible from developing thermal stress [58]. The small damage spot is observed at 5 mJ. Further increasing the laser irradiation, the large damage spot with heat distribution is formed around the spot. Microscopic damage patterns are shown in Fig. 24. The LDT value of the 2AP4N crystal was calculated using the following expression.

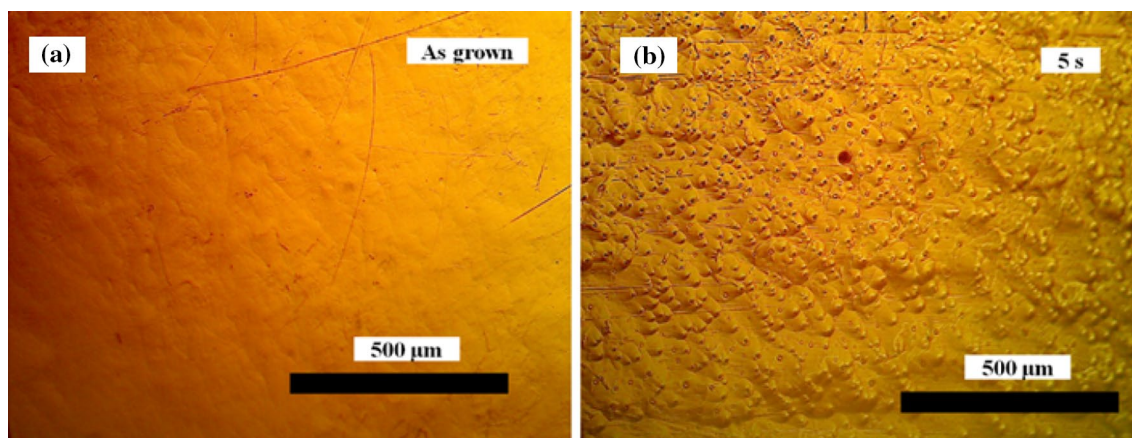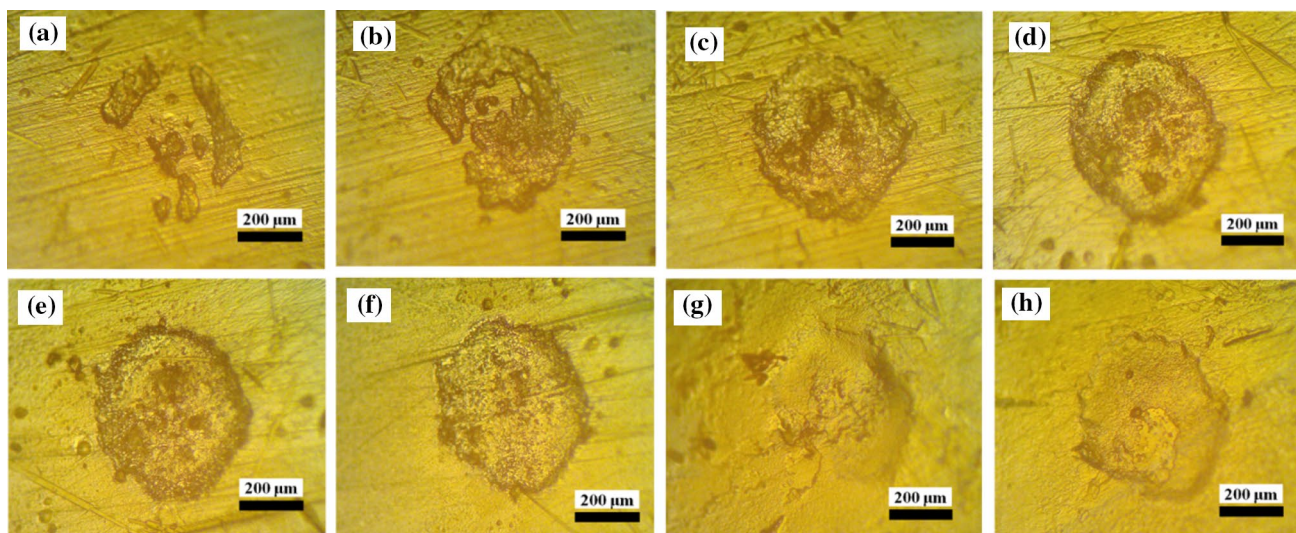$$\text{Power density}(P_d) = \frac{E}{\tau \pi (\omega_Z)^2} \tag{19}$$

Fig. 23 (**a**) As grown and (**b**) 5 s etched surface of 2AP4N crystal

Fig. 24 Microscopic images of the LDT patterns

where E is the input energy (mJ), τ is the pulse width (ns) and ω_Z is the radius of the beam on crystal surface as before the focal point and it can be calculated using the following expression:

$$\omega_Z = \omega_0 \sqrt{1 + \left(\frac{Z}{Z_R}\right)^2} \qquad (20)$$

$$Z_R = \left(\frac{\pi \omega_0^2}{\lambda}\right) \qquad (21)$$

where λ is the wavelength of laser (532 nm), f is the focal length of convex lens (10 cm) and d is the diameter of laser beam (8 mm) as before the convex lens. The value of ω_o was found to be 10 mm. The laser-induced bulk damage may occur due to many intrinsic factors arising from the optical behaviour of the materials and extrinsic factors such as material defects, impurities and surface roughness of the materials [59]. The LDT value of the grown 2AP4N crystal was found to be 3.12 GW/cm^2.

4.16 Second harmonic generation (SHG) analysis

The Kurtz–Perry powder technique is an extremely valuable tool for initial screening of the materials for analyzing second harmonic generation (SHG) efficiency [60]. The intense electromagnetic field of a laser radiation interacts with non-centrosymmetric crystals and it causes some polarizations of a crystal, then the new effect appears with linear response of the incident electric field. A Q-switched Nd: YAG laser beam ($\lambda = 1064$ nm) of input power of

10.8 mJ, and pulse width of 8 ns with a repetition rate of 10 Hz was used. The grown single crystal of 2AP4N was grained well and then it was packed in micro-capillary tube to expose the laser beams. Powder samples consist of a large number of randomly oriented crystals (including phase matching angle). The total SHG intensity of the powder samples is equal to the sum of the SHG intensity (interfered out) generated by each single particle. The intensity of green emission (532 nm) from the sample was collected using the monochromatic photo detector. The KDP is a standard material of this experiment. The SHG intensity of 2AP4N and KDP materials are shown in Fig. 25. Comparison of these intensities reveals that the 2AP4N is 4.5 times higher than that of KDP. The results suggested that the 2AP4N crystal is useful for SHG device applications.
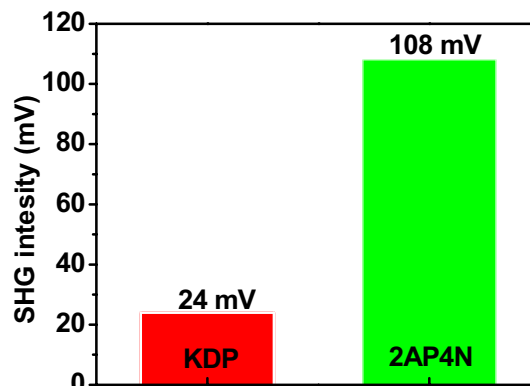
Fig. 25 Second-harmonic generation (SHG) efficiency

5 Conclusions

The optically high quality yellow colored organic NLO single crystals of 2-aminopyridinium 4-nitrophenolate 4-nitrophenol (2AP4N) have been grown by slow evaporation solution technique (SEST). The structure was confirmed by the SXRD analysis, it belongs to orthorhombic crystal system with space group of Pna2$_1$. The morphology has been indexed by WinXMorph software. The crystalline planes of the grown crystal were identified using Powder XRD and it was fitted using FullProf code. Quick quantitative insights and all the intermolecular interactions of the present 2AP4N crystal were revealed from 3D Hirshfeld surfaces and 2D fingerprint plots. The molecular vibrational spectra of FTIR and FT-Raman have been analyzed. UV–Vis NIR spectrum shows that the crystal is transparent in the visible and near IR regions with the lower cut-off wavelength of 470 nm. The band gap of the grown 2AP4N crystal was found to be 2.55 eV. The grown crystal has good optical transmittance and hence it is more suitable for NLO applications. The HOMO–LUMO energy value was analyzed and it was found to be 2.79 eV. The pictorial representation of molecule orbital compositions and their contributions to the chemical bonding (bonding, anti-bonding and non-bonding) have been analyzed. The hydrogen bond interactions in crystalline phase are evaluated by the Mulliken charge distributions of each atom. Molecular electrostatic potential and Mulliken charges are computed to know about the potential and charge distribution within molecule. In 2AP4N molecules, all the hydrogen atoms exhibited positive charge and all the oxygen atoms exhibited negative charge. The carbon and nitrogen atoms possess the both positive and negative charges. The intra and intermolecular bonding interactions have been investigated on 2AP4N molecule using NBO analysis and it provides a convenient orbital overlap between a lone pair of n$_1$(N$_2$) and antibonding of σ*(N$_1$–C$_3$) with stabilization energy of 84.47 kcal/mol. This high energy value leads to ICT interactions in a 2AP4N molecule. The first-order hyperpolarizability of the 2AP4N molecule has been calculated and it is 28.6 times greater than that of urea molecule. Photoluminescence reveals that the 2AP4N crystal has green emission (500 nm). Thermal studies indicated that the crystal was thermally stable upto 90 °C. There was no phase transition and decomposition below 90 °C. The chemical etching studies confirmed that the crystal has less dislocations. The higher value of laser damage threshold suggests that the grown crystals may be favorable for device applications. The Kurtz–Perry powder technique was carried out and the grown 2AP4N single crystals have good SHG efficiency compared with KDP. All the studies suggested that the grown 2AP4N single crystals are more suitable for frequency conversion, fluorescence detection in the visible range and LED applications.

References

1. P.N. Prasad, D.J. Williams, *Introduction to nonlinear optical effects in molecules and polymers*, 1st edn. (Wiley, New York, 1991)
2. D.S. Chemla, J. Zyss, *Nonlinear optical properties of organic molecules and crystals*, 1st edn. (Academic Press, London, 1987)
3. S. Ji, F. Wang, L. Zhu, X. Xu, Z. Wang, X. Sun, Sci Rep. **3**, 1605 (2013). https://doi.org/10.1038/srep01605
4. J. Zyss, *Molecular nonlinear optics materials, physics and devices* (Academic Press, New York, 1994)
5. C.H. McAteer, M. Balasubramanian, R. Murugan, in *Comprehensive heterocyclic chemistry III*, 7, ed. by A.R. Katrtzky, C.A. Ramsden, E.F.V. Scriven, R.J.K. Taylor (Elsevier, Oxford, 2008), pp. 309–336
6. V. Murugesan, M. Saravanabhavan, M. Sekar, Spectrochim Acta A **147**, 99–106 (2015). https://doi.org/10.1016/j.saa.2015.03.083
7. J. Hine, J. Am. Chem. Soc. **82**, 4877–4880 (1960). https://doi.org/10.1021/ja01503a031
8. T. Matsui, H.C. Ke, L.G. Hepler, Can. J. Chem. **52**, 2906–2911 (1974), https://doi.org/10.1139/v74-423
9. C.C. Evans, M. Bagieu-Beucher, R. Massse, J.F. Nicoud, Chem. Mater. **10**, 847–854 (1998). https://doi.org/10.1139/v74-423
10. K.S. Huang, D. Britton, M.C. Ettera, S.R. Byrn, J. Mater. Chem. **7**, 713–720 (1997). https://doi.org/10.1039/A604311J
11. S. Draguta, M.S. Fonari, A.E. Masunov, J. Zazueta, S. Sullivan, M.Y. Antipin, T.V. Timofeeva, CrystEngComm. **15**, 4700–4710 (2013). https://doi.org/10.1039/C3CE40291F
12. T. Chen, Z. Sun, L. Li, S. Wang, Y. Wang, J. Luo, M. Hong, J. Cryst. Growth **338**, 157–161 (2012). https://doi.org/10.1016/j.jcrysgro.2011.10.023
13. J. Pecaut, R. Masse, Acta Crystallogr. B **49**, 277–282 (1993). https://doi.org/10.1107/S0108768192008553
14. J.F. Nicoud, R.J. Twieg, D.S. Chemla, J. Zyss, *Nonlinear optical properties of organic molecules and crystals* (Academic Press, London, 1987)
15. M.J. Frisch, G.W. Trucks et al., Gaussian, Inc., Wallingford, CT, 2009
16. A. Frisch, A.B. Nielson, A.J. Holder, *GAUSS VIEW User's Manual* (Gaussian Inc., Pittsburgh, PA, 2000)
17. M.H. Jamr'oz, Spectrochim. Acta A **114**, 220–230 (2004)
18. N.M. O'Boyle, A.L. Tenderholt, K.M. Langner, J. Compos. Chem. **29**, 839 – 845 (2008). https://doi.org/10.1002/jcc.20823
19. M. Jaya Prakash, T.P. Radhakrishnan, Cryst. Growth Des. **5**, 721–725 (2005). https://doi.org/10.1021/cg049763e
20. G. Anandha babu, R. Perumal Ramasamy, P. Ramasamy, Mater. Chem. Phys. **117**, 326–330 (2009). https://doi.org/10.1016/j.matchemphys.
21. L.B. McCusker, R.B. Von Dreele, D.E. Cox, D. LoueEr, P. Scardi, J. Appl. Cryst. **32**, 36–50 (1999). https://doi.org/10.1107/S0021889898009856
22. E.R. Sokolowska, B. Marciniak, J. Ławecka, B. Bujnicki, J. Drabowicz, A. Rykowski, J. Sulfur Chem. **34**, 651–660 (2013). https://doi.org/10.1080/17415993.2013.799165

23. A.H. Reshak, D. Stys, S. Auluck, I.V. Kityk, Phys. Chem. Chem. Phys. **12**, 2975–2980 (2010). https://doi.org/10.1039/B920743K

24. C.F. Macrae, P.R. Edgington, P. McCabe, E. Pidcock, G.P. Shields, R. Taylor, M. Towler, J. van de Streek, J. Appl. Cryst. **39**, 453–457 (2006), https://doi.org/10.1107/S002188980600731X

25. J. Melsheimer, D. Ziegler, Thin Solid Films. **129**, 35–47 (1985). https://doi.org/10.1016/0040-6090(85)90092-6

26. S.J. Ikhmayies, R.N. Ahmad-Bitar, J. Mater. Res. Technol. **2**, 221–227 (2013). https://doi.org/10.1016/j.jmrt.2013.02.012

27. P. Karuppasamy, T. Kamalesh, V. Mohankumar, S. Abdul Kalam, M. Senthil Pandian, P. Ramasamy, S. Verma, S. Venugopal Rao, J. Mol. Struct. **1176**, 254–265 (2019). https://doi.org/10.1016/j.optmat.2018.07.039

28. K. Sankaranarayanan, P. Ramasamy, J. Cryst. Growth **280**, 467–473 (2005). https://doi.org/10.1016/j.jcrysgro.2005.03.075

29. J. Tauc, R. Grigorovici, A. Vancu, Phys. Status Solidi B **15**, 627–637 (1996). https://doi.org/10.1002/pssb.19660150224

30. P. Karuppasamy, V. Sivasubramani, M. Senthil Pandian, P. Ramasamy, RSC Adv. **6**, 109105–109123 (2016). https://doi.org/10.1039/C6RA21590D

31. A.L. Tenderholt, QMForge, Version 2.1; Stanford University: Stanford, CA, USA

32. E. Isac Paulraj, S. Muthu, Spectrochim. Acta A. **108**, 38–49 (2013). https://doi.org/10.1016/j.saa.2013.01.061

33. S. Muthu, E. Isac Paulraj, J. Mol. Struct. **1038**, 145–162 (2013). https://doi.org/10.1016/j.molstruc.2013.01.043

34. V. Balachandran, A. Lakshmi, A. Janaki, J. Mol. Struct. **1013**, 75–85 (2012). https://doi.org/10.1016/j.molstruc.2012.01.021

35. T. Uma Devi, R. Meenakshi, G. Kalpana, A. Josephine Prabha, J. Phys. Sci. **28**, 27–47 (2017). https://doi.org/10.21315/jps2017.28.1.3

36. T. Hughbanks, R. Hoffmann, J. Am. Chem. Soc. **105**, 3528–3537 (1983). https://doi.org/10.1021/ja00349a027

37. M. Chen, U.V. Waghmare, C.M. Friend, E. Kaxiras, J. Chem. Phys. **109**, 6680–6854 (1998). https://doi.org/10.1063/1.477252

38. S.I. Gorelsky, A.B.P. Lever, J. Organomet. Chem. **635**, 187–196 (2001). https://doi.org/10.1016/S0022-328X(01)01079-8

39. E.R. Davidson, S.X. Chakravarthy, Theo. Chim. Acta. **83**, 319–330 (1992). https://doi.org/10.1007/BF01113058

40. R.S. Mulliken, J. Chem. Phys. **23**, 1833–1840 (1955). https://doi.org/10.1063/1.1740588

41. S. Grimme, Zeitschrift für Physikalische Chemie. **205**, 136–137 (1654), https://doi.org/10.1524/zpch.1998.205.Part_1.136b

42. V.P. Gupta, *Principles and Applications of Quantum Chemistry*. (Elsevier, Amsterdam, 2016) pp. 195–214. https://doi.org/10.1016/B978-0-12-803478-1.00006-6

43. P. Politzer, D.G. Truhlar (eds.), *Chemical Applications of Atomic and Molecular Electrostatic Potentials* (Plenum Press, New York, 1981)

44. J.P. Foster, F. Weinhold, J. Am. Chem. Soc. **102**, 7211–7218 (1980). https://doi.org/10.1021/ja00544a007

45. M. Snhelatha, C. Ravikumar, I. Hubertjoe, N. Sekar, V.S. Jayakumar, Spectrochim. Acta. A. **72**, 654–662 (2009), https://doi.org/10.1016/j.saa.2008.11.017

46. R.I. Al-Wabli, A. Salman, V. Shyni, H.A. Ghabbour, I. Hubert Joe, M.S. Almutairi, Y.A. Maklad, M.I. Attia, J. Mol. Struct. **1155**, 457–468 (2018). https://doi.org/10.1016/j.molstruc.2017.10.116

47. A.E. Reed, F. Weinhold, J. Chem. Phys. **78**, 4066–4073 (1983). https://doi.org/10.1063/1.445134

48. J. Chocholou sova, V. Spirko, P. Hobza, Phys. Chem. Chem. Phys. **6**, 37–41 (2004). https://doi.org/10.1039/B314148A

49. R. Rahmani, N. Boukabcha, A. Chouaih, F. Hamzaoui, S. Goumri–Said, J. Mol. Struct. **1155**, 484–495 (2018). https://doi.org/10.1016/j.molstruc.2017.11.033

50. C.S. Abraham, J.C. Prasana, S. Muthu, Spectrochim. Acta A **181**, 153–163 (2017). https://doi.org/10.1016/j.saa.2017.03.045

51. D.R. Kanis, M.A. Ratner, T.J. Marks, Chem. Rev. **94**, 195–242 (1994). https://doi.org/10.1021/cr00025a007

52. D.A. Kleinmann, Phys. Rev. **126**, 1977–1979 (1962). https://doi.org/10.1103/PhysRev.126.1977

53. D.C. Harris, M.D. Bertolucci, *Symmetry and Spectroscopy, An Introduction to Vibrational and Electronic Spectroscopy* (Dover Publications, Inc., New York, 1989)

54. J. Dalal, N. Sinha, H. Yadav, B. Kumar, RSC Adv. **5**, 57735–57748 (2015). https://doi.org/10.1039/C5RA10501C

55. E.S. Rorem, J. Chromatogr. A. **4**, 162–165 (1960), https://doi.org/10.1016/S0021-9673(01)98388-8

56. G. Om Reddy, K.S. Ravikumar, Thermochim. Acta **198**, 147–165 (1992). https://doi.org/10.1016/0040-6031(92)85069-8

57. V.V. Azarov, L.V. Atroshchenko, Y.K. Danileiko, M.I. Kolybaevs, Y.P. Minaev, V.N. Nikolaev, A.V. Sidorin, B.I. Zakharkin, Sov. J. Quantum Electron. **15**, 89–90 (1985). https://doi.org/10.1070/QE1985v015n01ABEH005862

58. K.E. Montgomery, E.P. Milanovich, J. App. Phys. **68**, 3979 (1990). https://doi.org/10.1063/1.346259

59. H. Yoshida, H. Fujita, M. Nakatsuka, M. Yoshimura, T. Sasaki, T. Kamimura, K. Yoshida, J. Appl. Phys. **45**, 766 (2006), https://doi.org/10.1143/JJAP.45.766

60. S.K. Kurtz, T.T. Perry, J. App. Phys. **39**, 3798 (1968). https://doi.org/10.1063/1.1656857